Inviscid Computation of Effect of Wake Vortices on a Scale-Model Airplane

R. Struijs,[*] G. Jonville,[*] and D. Darracq[*]
Centre Européen de Recherche et de Formation Avancée en Calcul Scientifique, 31057 Toulouse Cedex 01, France
and
R. Heinrich[†]
DLR, German Aerospace Research Center, 38108 Brunswick, Germany

The forces and moments sustained by a scale-model airplane in the wake of another aircraft have been calculated using two different solvers. One solver uses a fourth-order central scheme with a specially adapted grid, whereas the other uses a chimera technique with second-order discretization. Additionally, simplified models were used on grids that are too coarse to represent vortices properly. These models work by handling the effect of the vortices by modifying the flux at the solid wall, or the fluxes in the domain. The experimental flowfield that contains wake vortices is modeled by a least-square fit analytical expression. This description is used as the inlet boundary condition for the Euler solvers. Numerical results are in agreement with experiment and with previously published computations using panel methods.

I. Introduction

TO avoid risks for an aircraft flying in the wake vortex field of a preceding aircraft, strict rules for minimum required separation distances have been devised. They are merely based on the weight of the aircraft and do not take into account details of the wake formation, the influence of specific meteorological conditions on the far wake evolution, and the recovering capabilities of the following aircraft. Despite very conservative International Civil Aviation Organization separation distances between airplanes at takeoff and landing, encounter between wake turbulence of a leading aircraft with a following aircraft can occur in certain circumstances, leading to dramatic accelerations and loss of control. To find more realistic separation rules, the wake vortex evolution and wake vortex encounter project addresses the topics mentioned above. Experimental investigations have been carried out to get a better understanding not only of the vortex evolution behind an aircraft but also of the encounter with the following aircraft. Measurements with real aircraft have been made, but the experiment is dangerous and circumstances are difficult to control. Wind-tunnel measurements have been made in well-defined conditions, but are limited in the separation length between the aircraft and are also restricted in Reynolds number.

Our purpose is to compare three-dimensional steady-state inviscid computations with the experimental results. The first Euler computations about a full aircraft appeared about 15 years ago. Since then, a continuing increase of computing capacity has made Navier–Stokes solutions possible, together with a variety of turbulence models. However, a simulation of a wake–vortex encounter poses some additional problems. The validity of turbulence models is questionable for an application with highly vortical flow with unpredictable and possibly strong separation, and it is difficult to foresee which part of the domain has to be covered by a fine mesh. Also the vortices generated by the leading aircraft have to be properly resolved, increasing further the strain on computational resources. Very few

computations can be found in literature on a wake–vortex encounter. Some work has been done with panel methods, but very little with Euler or Navier–Stokes solvers. As an example of the latter, see Ref. 1, where a thin-layer Navier–Stokes computation is made of the flowfield of a wake generating wing and its effect on a trailing wing. The authors use a two-layer Baldwin–Lomax turbulence model, which was specially designed for attached and mildly separated flows. Although these computations are recent, the grid is quite coarse. Ting and Lan report insufficient vortex resolution and underestimation of the rolling moment coefficients.

In these circumstances, an Euler simulation of a wind-tunnel experiment is useful. The absence of viscous terms and turbulence introduces errors, but their magnitude may be negligible because the huge aerodynamic forces dominate the encounter. The computation will reveal to which extent this assumption is true and will give an idea about the accuracy of the simulation. Beforehand, the results may be expected to be of better quality than those obtained with panel methods.

The starting point of the present investigation is a wake vortex encounter experiment, which has been performed in the Deutsch–Niederländischer Windkanal (German–Dutch wind tunnel) large low-speed facility (DNW-LLF).[2] A wake-generating model creates a flowfield with a pair of counter-rotating wing-tip vortices. The flowfield has been measured with a rake of five-hole probes. Next, the rake was replaced by a model airplane with a wing span of about half of that of the upstream airplane. Forces, moments, and pressure distributions have been measured at several model positions in the vortex disturbed flowfield. This well-controlled experiment produces accurate data over a large domain with high resolution. It constitutes an excellent database for the validation of simulation codes aiming at representing qualitatively and quantitatively the effects of wake vortex encounters. All measurements were made at the same velocity $M = 0.17$ and, hence, the same Reynolds number of about 2.3×10^5 based on the chord of the following aircraft.

The measurements of the flowfield with the rake will be used as the inlet condition for a computation. The first part of this paper consists of modeling, that is, a representation of the experimental flowfield using simple analytical functions (Sec. II). Next, in Sec. III, the inviscid flowfield is calculated at some positions and compared with experimental results. Adequate resolution of the wake vortices is important, and the capabilities of two different codes are tested: a Navier–Stokes multiblock (NSMB) solver from the Centre Européen de Recherche et de Formation Avancée en Calcul Scientifique (CERFACS) and a solver with the name FLOWer from DLR,

German Aerospace Research Center. The first uses a fourth-order central scheme with a specially adapted grid, and the second uses a chimera technique with second-order discretization.

II.   Representation of the Experimental Flowfield

To compute the effects of the wake vortices on the scale-model airplane, the numerical methods need upstream boundary conditions that represent the experimental flowfield as accurately as possible. Therefore, we will start by analyzing in detail the experimental flowfield.

In the experiment,[2] measurements are made 13 wing spans downstream of a wake-generating model, a Fokker F29 without flaps or empennage with a wing span of 1.30 m at $\alpha = 9$ deg. The follower model, subsonic wall interference model (SWIM) has a tail sting support, straight untwisted wings, and horizontal and vertical tail sections. It is mounted without flaps at zero angle of attack. The NACA 4412 wing has a span of 0.6 m, and the mean chord is 0.075 m. The setup of the experiment is indicated in Fig. 1. Velocities and pressure have been measured in the plane perpendicular to the mean flow. The grid spacing for the measurements is 7.5 mm. The measured flowfield is smaller in extent than the computational domain, and the modeled flow should approach the measured flow as close as possible. The modeling will be split in two parts. First, the crossflow components will be treated, and separately, the streamwise component will be modeled.

A.   In the Crossflow Plane

An example of the measured flow for the port vortex is given in Fig. 2. The axes notation of Ref. 2 is used, that is, positive x for the downstream direction and y and z for horizontal and vertical directions with respect to the tunnel, with velocities u, v, and w,

respectively. As mentioned in Ref. 2, the global flowfield consists of two strong counter-rotating wing-tip vortices and two weaker spurious ones.

Our aim is to represent the experimental flowfield with simple analytical functions, which can be used as inlet boundary condition for a computation. The complex flowfield we encounter excludes an analytical representation that is a solution of the Navier–Stokes equations. The best we can do is add a number of vortices, each of which is by itself a solution of the Navier–Stokes equations. For weakly interacting vortices, the approximation will be acceptable. Furthermore, in an inviscid computation, the viscous effects are due to the numerical scheme instead of the viscosity of the fluid.

To get an idea of the quality of the modeling we need, we consider the effect of a possible systematic error in the vertical velocity. This will have the effect of an apparent angle of attack, and the lift polar that depicts lift vs angle of attack, Fig. 3 (also see Ref. 2) gives us the corresponding error in the lift coefficient C_L. For a freestream velocity of 59 m/s, an error of the vertical velocity of 1 m/s, or 1.7% of the freestream velocity, results in an angle of attack of about 1 deg and an error in the lift coefficient C_L of 0.1. Such an error for C_L is quite large. Therefore, the desired accuracy puts a constraint on the analytical functions.

An analytical vortical solution is easiest represented in cylindrical coordinates (r, θ, z). The azimuthal velocity $V_\theta(r, t)$ should satisfy the incompressible unsteady Navier–Stokes equations,

$$\frac{\partial V_\theta}{\partial t} = \nu \left(\frac{\partial^2 V_\theta}{\partial r^2} + \frac{1}{r} \frac{\partial V_\theta}{\partial r} - \frac{V_\theta}{r^2} \right) \tag{1}$$

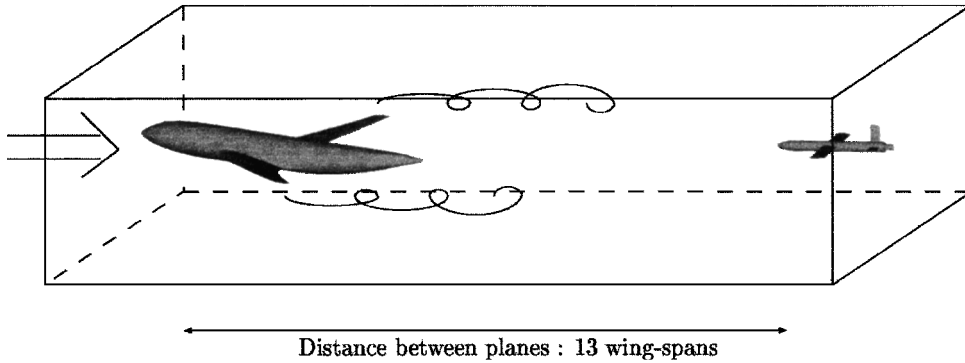$$\frac{V_\theta^2}{r} = \frac{1}{\rho} \frac{\partial p}{\partial r} \tag{2}$$

Fig. 1   Experimental setup in DNW-LLF wind tunnel; upstream wake-generating model creates wing-tip vortices, which are interacting with the downstream model.
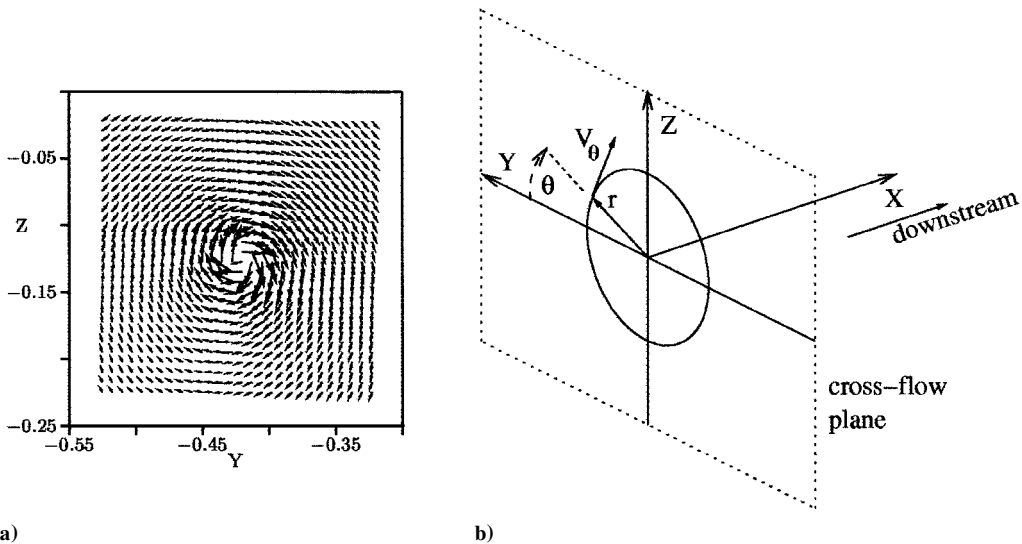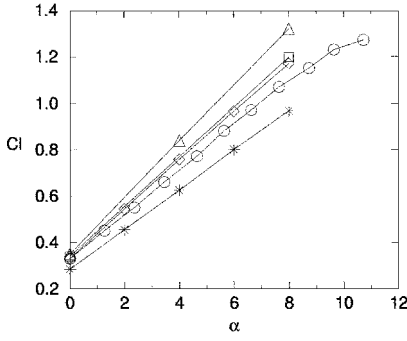

a)   b)

Fig. 2   Experimental flowfield around the port vortex and the axis system used: a) velocity vector plot and b) axis.

Fig. 3 Lift coefficient C_L vs angle of attack α; experimental results of DNW and computations: $\bigcirc$, DNW experiment; $\triangle$, NSMB; $\diamond$, FLOWer coarse grid; $\square$, FLOWer fine grid; and $*$, PDAERO.

with ν the kinematic viscosity, ρ the density, and p the pressure. A well-known analytical vortical solution is given by Lamb and Oseen (see Ref. 3),

$$V_\theta(r, t) = V_m \alpha (r/r_c)^{-1} \left\{ 1 - \exp\left[-\beta(r/r_c)^2\right] \right\} \qquad (3)$$

where the time dependence is present in the core radius $r_c(t) = \sqrt{(\beta 4 \nu t)}$. For $r \ll r_c$, $V_\theta \sim r$, which corresponds to a solid-body rotation. In the far field, $r \gg r_c$, and $V_\theta \sim r^{-1}$. At the core radius r_c, V_θ reaches its maximum V_m. Consequently, the parameters α and β satisfy

$$-e^\beta + 2\beta + 1 = 0, \qquad \alpha = 1/(1 - e^{-\beta}) \qquad (4)$$

so that $\beta \approx 1.25$ and $\alpha \approx 1.40$.

As mentioned in Ref. 4, studies of inviscid rollup of vortex sheet show far-field decay of $V_\theta \sim r^{-n}$ with n any real positive or negative number. The rollup of an edge in uniform motion has $V_\theta \sim r^{-1/2}$. Modeling the experimental velocity field by means of the Lamb–Oseen vortex (see Ref. 3), which has an $1/r$ decay, is, therefore, unfeasible.

Analytical formulation of more general vortical solutions to the Navier–Stokes equations has been derived by Kirde.[5] The starting point is a dimensional analysis, which leads to a relevant parameter $x = r^2/4\nu t$, commonly used in the derivation of the Lamb–Oseen vortex (see Ref. 3). Linear variation of V_θ near the core and far-field variation $V_\theta \sim r^n$ with separation of variables lead to a solution in the form of a confluent hypergeometric series[4,5]

$$V_\theta(r) = V_k r_1 F_1[(1 - n)/2; 2; -x] \qquad (5)$$

where V_k is a scaling factor.

The fit of a model to experimental data is performed with ODRPACK.[6] This package solves the weighted orthogonal distance regression problem, that is, it minimizes the sum of the squares of the weighted orthogonal distances between each data point and the curve described by the model equation. This way we obtain the relevant parameters as amplitude, core radius, and position.

Equation (5) is not very practical for use with ODRPACK. Implementations of confluent hypergeometric series are available,[7] but need to be used with care. Instead, we generalize Eq. (3) for the approximation of the analytical solution. It maintains the limiting behavior for extreme values of r,

$$V_\theta(r, t) = V_m \alpha (r/r_c)^{-\gamma} \left\{ 1 - \exp\left[-\beta(r/r_c)^{1+\gamma}\right] \right\} \qquad (6)$$

where now

$$-e^\beta + (1 + 1/\gamma)\beta + 1 = 0, \qquad \alpha = 1/(1 - e^{-\beta}) \qquad (7)$$

For $\gamma = \frac{1}{2}$, $\beta \approx 1.90$ and $\alpha \approx 1.18$. This generalization is not a solution of Eq. (1), but rather an engineering approximation to the analytical solution of Eq. (5). However, the normalized plot of both functions in Fig. 4, shows that Eq. (6) is a good approximation for practical purposes.

Table 1 Parameters used in the reconstruction of the experimental flowfield

Vortex	V_m, m/s	r_c, mm	y_0, m	z_0, m
Port (wing tip)	21.0	5	−0.420	−0.126
Port (spurious)	3.3	50	−0.561	−0.510
Starboard (wing tip)	21.0	5	0.390	−0.090
Starboard (spurious)	3.3	50	0.531	−0.514
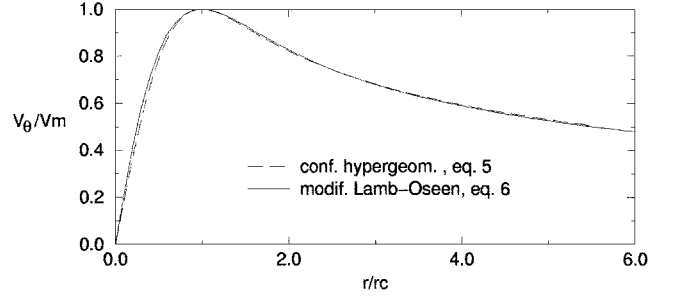
Fig. 4 Comparison of analytical vortices, hypergeometric vs modified Lamb–Oseen (see Ref. 3) general analytical vortical solution and an approximation for $n = -\gamma = -1/2$.

The flow contains two strong wing-tip vortices due to the rollup of the vortex sheet and two spurious weak vortices with the same sense of rotation as the main vortices. The spurious vortices are slightly outbound and below the wing-tip vortices (Table 1). In the first instance, an attempt was made to model the experimental flowfield with four vortices. It turns out that this is not sufficient to achieve the desired accuracy. If we take the experimental flowfield and subtract the effect of the four vortices, the remaining field contains large velocity components varying over a great distance. These components, of the order of 3–4 m/s, or some 5–7% of the freestream velocity, may be due to the tunnel walls or to the wake-generating model. The isolines of the vertical velocity component w of the remaining field are given in Fig. 5. A cut of the vertical component w and the horizontal velocity component v at various vertical z positions is given in Figs. 6 and 7. The w component is roughly symmetric about the $y = 0$ plane, varying linearly with y, but also with z. The horizontal velocity v varies less regularly. For modeling purposes, we assume it also linear with y and independent of z. This is obviously not true, but it gives a reasonable fit for $z = -0.1$, where the model plane is positioned.

A fair reconstruction of the experimental flowfield consists of four vortices given by Eq. (6) ($\gamma = \frac{1}{2}$) and Table 1, together with linearly varying fields of the following equations:

$$v(y, z) = -0.07 + [(y + 1.72)/1.72]0.90 \text{ m/s} \qquad (8)$$

$$w(y, z) = 3.70 - |y/1.14|2.80$$
$$+ [(z + 0.6145)/0.765](-0.9) \text{ m/s} \qquad (9)$$

The 95% uncertainty errors estimated by ODRPACK are about 3% for the vortex strength, 1% for the core radius, and an uncertainty of about 5 mm for the position of the core.

Subtracting this analytical field from the experimental data results in the flowfields that are shown in Figs. 8a–8c. A residual of the core of the wing-tip vortices is visible, but the blowup of the cores in Figs. 8b and 8c shows that no overall vortical structure remains. The field at the core has maximal velocities of about 6 m/s, but the flow is fairly random. Several attempts were made to reduce these residuals. The vortex parameters were varied (origin, core radius, and strength), but without improvement of the fit. It is mentioned in Ref. 2 that velocity measurement errors in normal circumstances are about 2 m/s and that the error may increase near the core, but it is not clear if this explains these magnitudes. The resulting fields (Fig. 8)
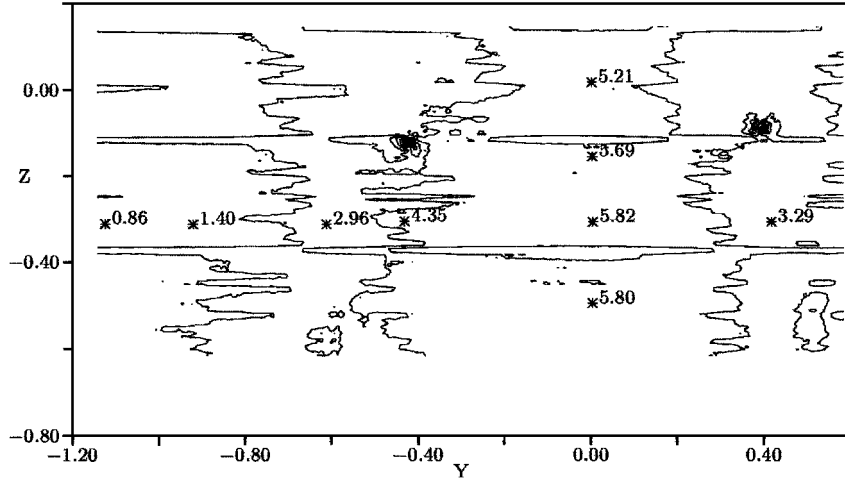
Fig. 5 Isolines of vertical velocity component *w* after elimination of the vortices; asterisks indicate some values as percentage of the freestream velocity.
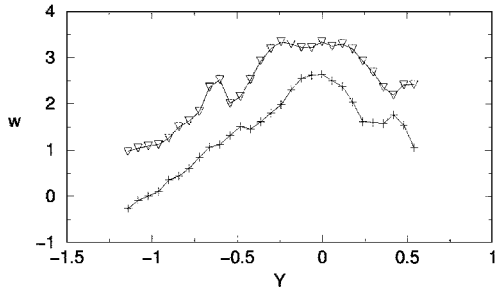

Fig. 6 Cut of the vertical velocity component *w* given as a percentage of the freestream velocity, as a function of the horizontal coordinate *y* for different values of the vertical coordinate *z*, after elimination of the vortices: ∇, $z = -0.6$ and $+$, $z = 0$.
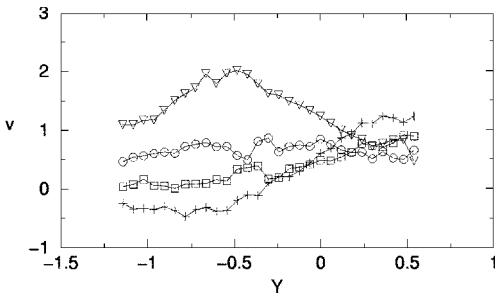

Fig. 7 Cut of the horizontal velocity component *v* given as a percentage of the freestream velocity, as a function of the horizontal coordinate *y* for different values of the vertical coordinate *z*, after elimination of the vortices: ∇, $z = -0.6$; $\bigcirc$, $z = -0.4$; $\square$, $z = -0.2$; and $+$, $z = 0$.

show clearly the systematic errors of the individual probes in the rake. These errors are in the order of magnitude of 1 m/s and are already visible in the flow visualization of Fig. 20 of Ref. 2. Using the experimental flow field directly as inlet boundary condition implies accepting these systematic errors.

Finally, we wanted to see whether it was appropriate to use Eq. (6) to model the vortices instead of Eq. (3). We subtracted from the experimental field the strong and weak starboard vortices, the weak port vortex, and the linear fields. This leaves us with the strong port vortex. Next, for the domain $(-0.62, -0.22) \times (-0.32, 0.08)$, that is, a square around the port vortex, a plot of the azimuthal velocity has been made (Fig. 9). In Fig. 9, two analytical vortices have been fit. The modified Lamb–Oseen vortex provided by Eqs. (6–9) fits the data set very well, for all values of *r*. For this fit, we used the

parameters in Table 1. It is not possible to get a good fit with the standard Lamb–Oseen vortex, (see Ref. 3), Eq. (3). The package ODRPACK finds now $V_m = 17$ m/s and $r_c = 0.02$ m, both with an error of more than 50%. The reason is that the experimental data exhibit a $1/\sqrt{r}$ decay in the far field, and the best Lamb–Oseen (see Ref. 3) fit taking into account all of the data results in an overestimation of r_c and an underestimation of V_m. For modest values of *r*, a better fit with the Lamb–Oseen vortex is possible reducing the value of r_c and increasing V_m. However, then the discrepancy for large values of *r* becomes unacceptable.

The reconstruction of Eqs. (6–9) with the parameters in Table 1 is used for the computations in Sec. III.

B. In Streamwise Direction

In Fig. 10, the *u* velocity distribution around the port vortex is plotted. The influence of the azimuthal velocity component V_θ is felt far from the core, whereas the axial velocity *u* becomes uniform very fast. Given the spread in the experimental data, and the relative short range where the deviation from the freestream value is important, the axial velocity component *u* is modeled in much less detail than the azimuthal field. For the continuous curve in Fig. 10, we took

$$V_{ax}(r) = V_f + V_{ma} \exp\left[-\beta (r/r_{ca})^{1+\gamma}\right] \tag{10}$$

where V_f is the freestream axial velocity and V_{ma} calibrates the peak value of the axial velocity at the center of the vortex. The axial radius r_{ca} is different from the core radius r_c. This equation is inspired by Ref. 8, although the dependence on the radius is modeled after Eq. (6). The values applied are

$$V_f = 59 \text{ m/s}, \qquad V_{ma} = -22 \text{ m/s}$$

$$r_{ca} = 0.012 \text{ m}, \qquad \gamma = \tfrac{1}{2} \tag{11}$$

The same values were used for the starboard vortex. No modeling has been applied for the axial velocities of the spurious vortices because the effects are likely to be minimal.

III. Computation of the Flowfield with Euler Solvers

In the experiment described in Sec. II, the trailing aircraft was placed at several positions in the vortical flowfield of a preceding aircraft. For the computation, we select five positions to compare numerical results with experimental data. They correspond to traverse four of the experiment described in Ref. 2. The model positions relative to the preceding aircraft are shown in Fig. 11, looking in
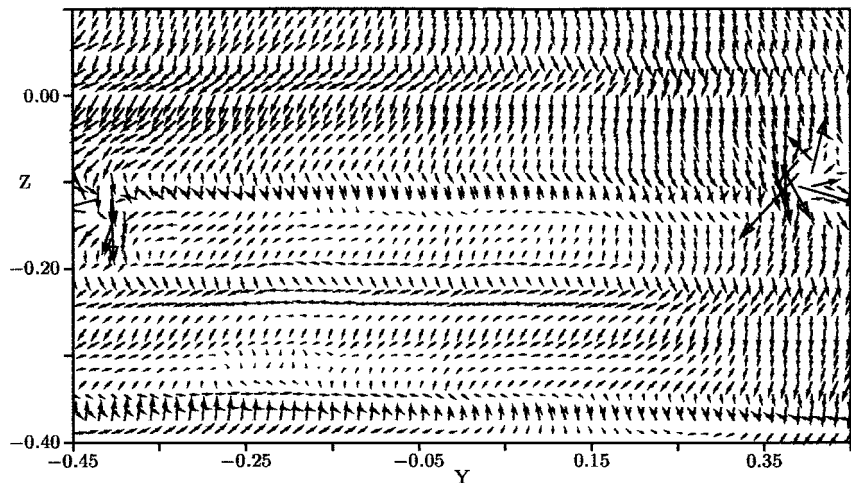
Fig. 8a   Velocity vector plot of residual flowfield after subtracting vortices and linear components; field between the wing vortices is shown with only every second point in each direction.
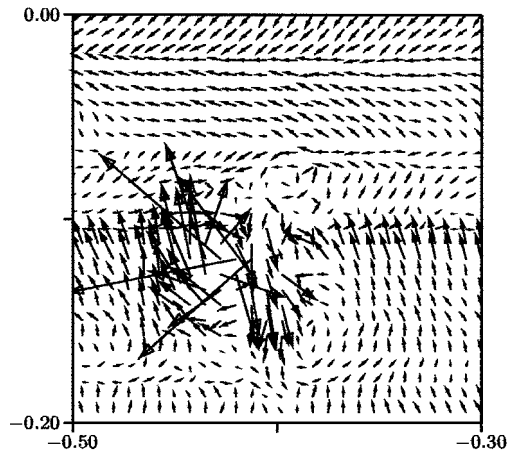

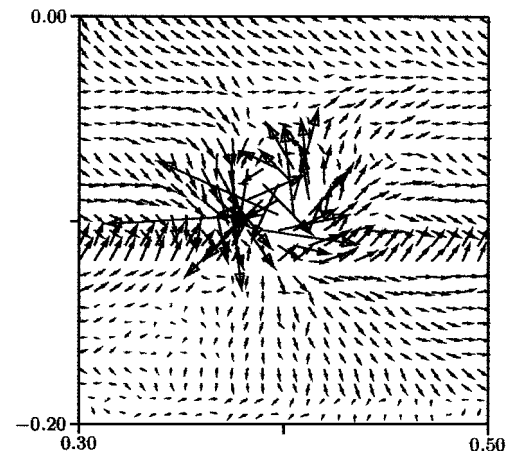Fig. 8b   Velocity vector plot of blowup around the port vortex.
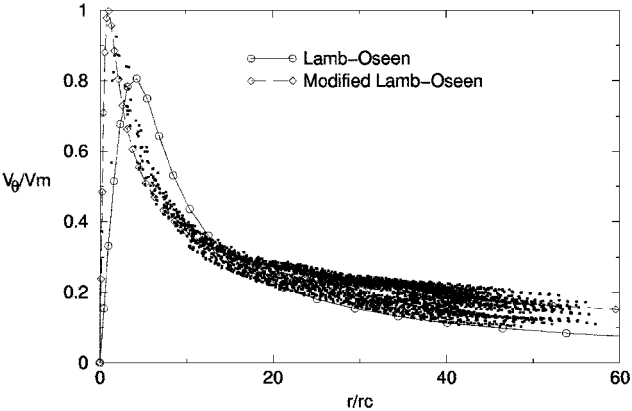

Fig. 9   Azimuthal velocity V_θ around the port vortex; Lamb–Oseen vortex [Eq. (3)] and modified Lamb–Oseen vortex with $\gamma = 0.5$ [Eq. (6)] fitted to experiment. Nondimensionalization is by the values of V_m and r_c of the modified Lamb–Oseen vortex (see Ref. 3).
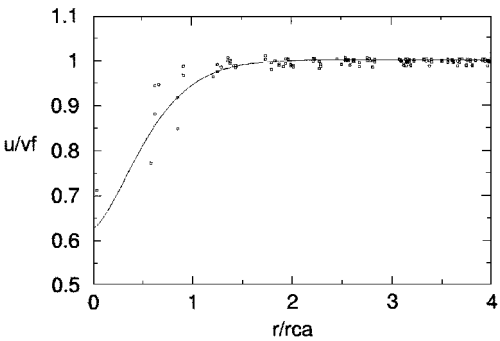

Fig. 8c   Blowup around the starboard vortex.

Fig. 10   Axial velocity u around the port vortex; velocity is scaled by freestream velocity v_f, and the distance r is scaled by axial core radius r_{ca}.

the flight direction (negative x direction). This particular selection enables us to catch the extremes in lift and roll.

The effect of the upstream plane on the downstream model is computed by solving the Euler equations. Although the grid requirements for Euler computations are in general less severe than for Navier–Stokes computations, a proper resolution of the vortices is needed. A vortex on a coarse mesh will be seen by the solver as a collection of steep gradients, which will rapidly be smeared out.

Therefore, a relatively fine mesh is needed locally to resolve the vortices from the inlet boundary to the airplane. When the vortices hit an obstacle, they will be deflected and deformed. They have the liberty to do so, because they have been imposed only far upstream.

The grid constraints can be further reduced using simplified methods, which work on nonrefined meshes. As already mentioned, when the vortices are imposed at the upstream inlet of the domain, they will have disappeared upon arrival at the airplane due to the diffusive properties of the numerical method. Their effect on the airplane in the simplified methods is, therefore, introduced via the boundary conditions at the solid wall of the scale-model airplane, or via
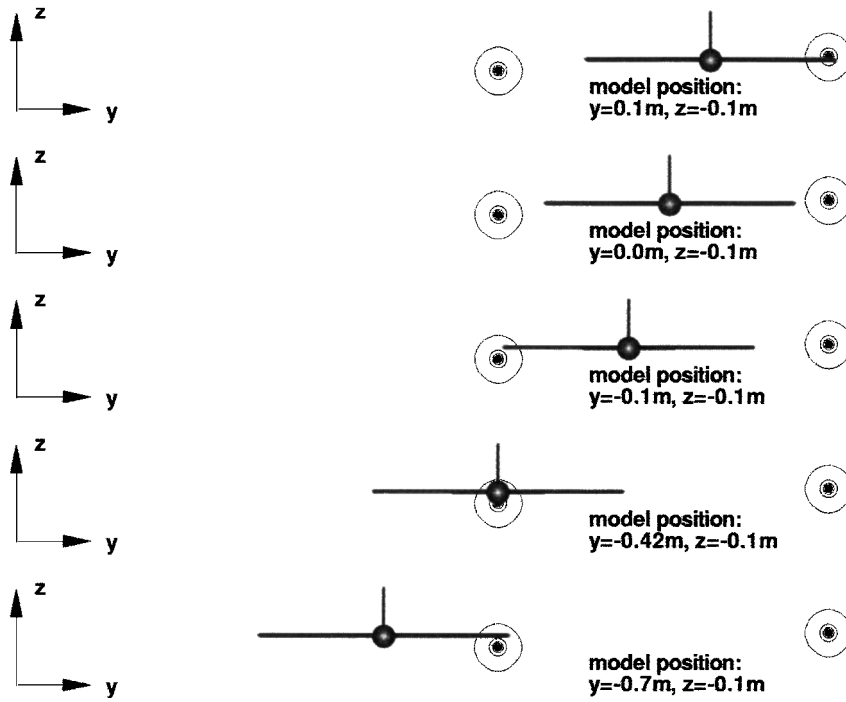
Fig. 11 Selected cases for wake encounters of SWIM geometry (looking in flight direction).

modified flux calculations inside the domain. However, because the vortices are specified locally, close to the following aircraft, their liberty to deform or to deflect is strongly reduced . This may introduce errors, especially for strong interactions.

Two different parallel multiblock codes are used that implement the solution strategies mentioned.

1) NSMB (CERFACS) uses a fourth-order central scheme with an implicit lower–upper symmetric Gauss–Seidel for time integration. (NSMB is jointly developed with the École Polytechnique Fédérale de Lausanne in Switzerland; the Royal Institute of Technology in Stockholm, Sweden; Aérospatiale Matra Airbus in Toulouse, France; and SAAB, in Sweden.) The fourth-order scheme reduces the need for very fine meshes. Technical details may be found in Refs. 9 and 10.

2) FLOWer (DLR) uses a second-order Jameson-type central scheme with a chimera grid technique that enables easy local, grid refinement and a five-stage Runge–Kutta time integration with multigrid. Additionally, simplified and arbitrary Lagrangian–Eulerian (ALE) methods are available to account for the effect of vortices on nonrefined meshes. For more information, see Refs. 11–16 and the references cited therein.

The chimera overset grid approach implemented in FLOWer involves the decomposition of a complex geometry into a number of geometrically simple overlapping grids. There are several incentives for employing an overset grid approach for steady or unsteady three-dimensional flows. The flow solution process is applied to topologically simple grids. The component meshes, which are well suited for vortex dominated flows, can be embedded into Cartesian background meshes. All of the advantages associated with structured data are kept in the approach, including highly efficient implicit flow solvers, vectorization, and parallelism.

It is in fact very easy to adapt an existing multiblock flow solver of documented accuracy and efficiency to use overset grids, which is a major advantage of the chimera method. Examples of applications using the chimera technique may be found in Refs. 13–16.

A. Lift in Uniform Flow

Before the expensive encounter computations were performed, the quality of the mesh was checked by simulations of the model in uniform flow for a set of angles of attack. Only the half-model has been considered, due to the symmetrical character of the flow. The
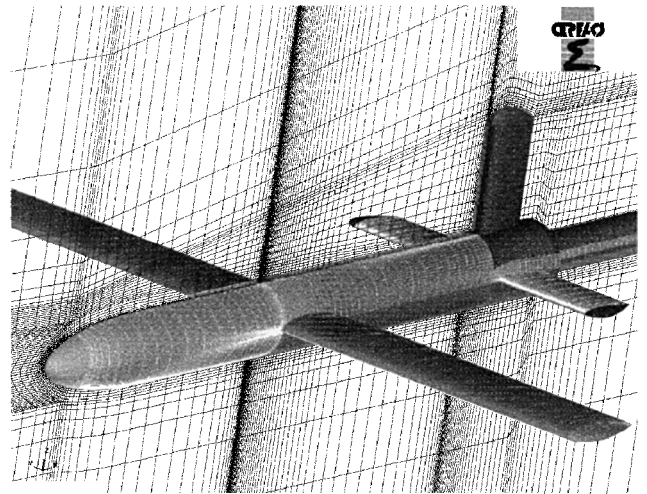

Fig. 12 The grid for the model plane, used with NSMB.

grids are shown in Fig. 12 for NSMB and in Figs. 13a and 13b for FLOWer. In Fig. 12, the domain $(-1.0, 1.0) \times (0., 1.0) \times (-1.0, 1.0)$ with the origin at the model reference point is discretized with about 8×10^5 nodes for the half-grid. The grids for FLOWer of Fig. 13 employ the chimera technique. Component meshes have been generated separately around the fuselage, the wings, and the horizontal and vertical tails. The whole structure is embedded in a Cartesian background mesh. Two half-grids have been generated, a coarse grid with 2.12×10^5 nodes and a fine grid with 1.7×10^6 nodes. For the SWIM geometry without vertical tail, experimental data are available. Because FLOWer uses a chimera mesh, there was no problem in removing the vertical tail component mesh from the computation. Five computations were performed for angles of attack $\alpha = 0, 2, 4, 6$, and 8 deg on the coarse mesh and two on the fine mesh for $\alpha = 0$ and 8 deg. Two multigrid levels were used for convergence acceleration, and 500 iterations were sufficient to reach a convergence of four orders of magnitude for FLOWer. For NSMB, the model with vertical tail is taken at three different angles of incidence, $\alpha = 0, 4$ and 8 deg. At the far-field boundary, nonreflecting boundary conditions were used. The Mach number is 0.174.
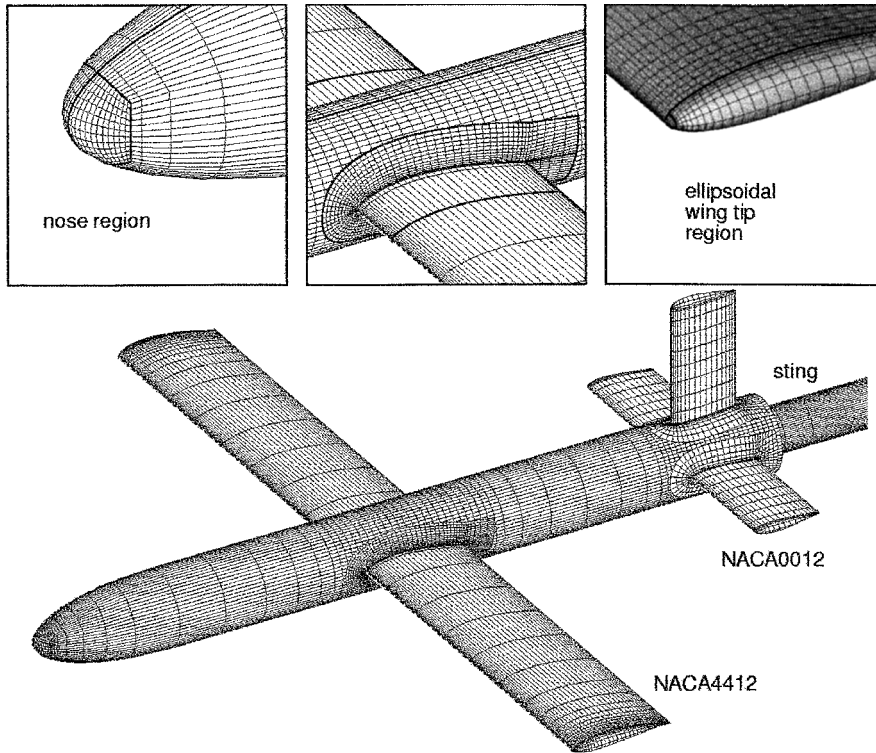
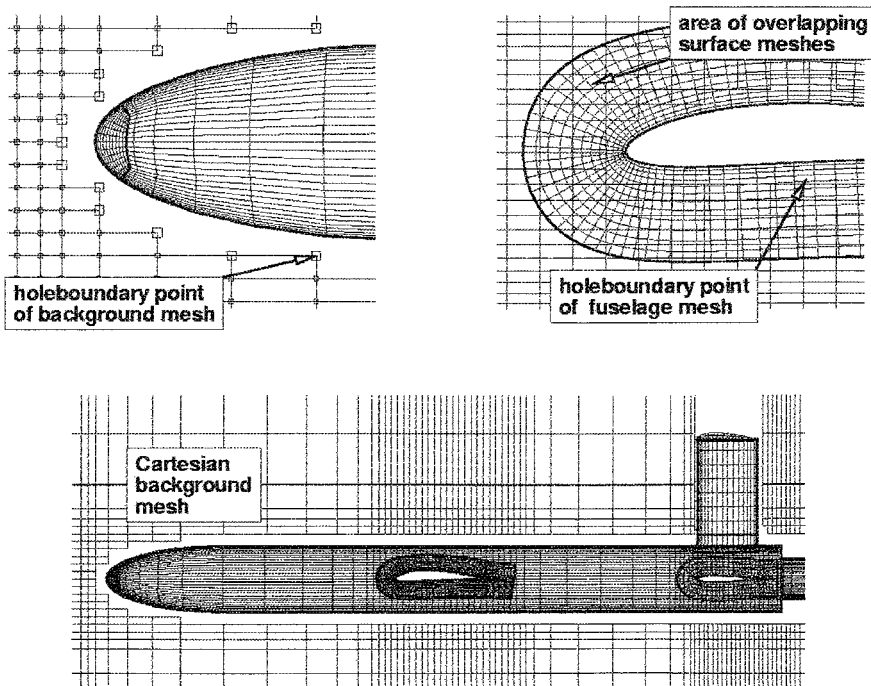Fig. 13a   Overview of component meshes of the SWIM geometry (every third mesh line), used with FLOWer.

Fig. 13b   Background mesh and some details of the SWIM geometry (xz plane, every third grid line).

Figure 3 shows the comparison of the numerical results and the DNW experiment. All Euler computations overestimate lift, whereas the panel method PDAERO[17] underestimates lift. The DLR computations using the chimera mesh are closer to the experimental data. The difference between both fine and coarse chimera meshes is relatively small. The overestimation of the lift, especially for the high angles of attack, is influenced by viscous effects.

B.   Computation of Vortical Flowfields

As mentioned earlier, one of the main problems in computing wake–vortex interactions with Euler and Navier–Stokes solvers is the convection of the vortex from the inflow boundary to the model without large numerical losses. At the far-field inlet, grids usually have coarse cells with sizes that exceed the core radius r_c of a vortex by several orders of magnitude. Therefore, the resolution of the grid near the core needs adjustment. The chimera technique of FLOWer
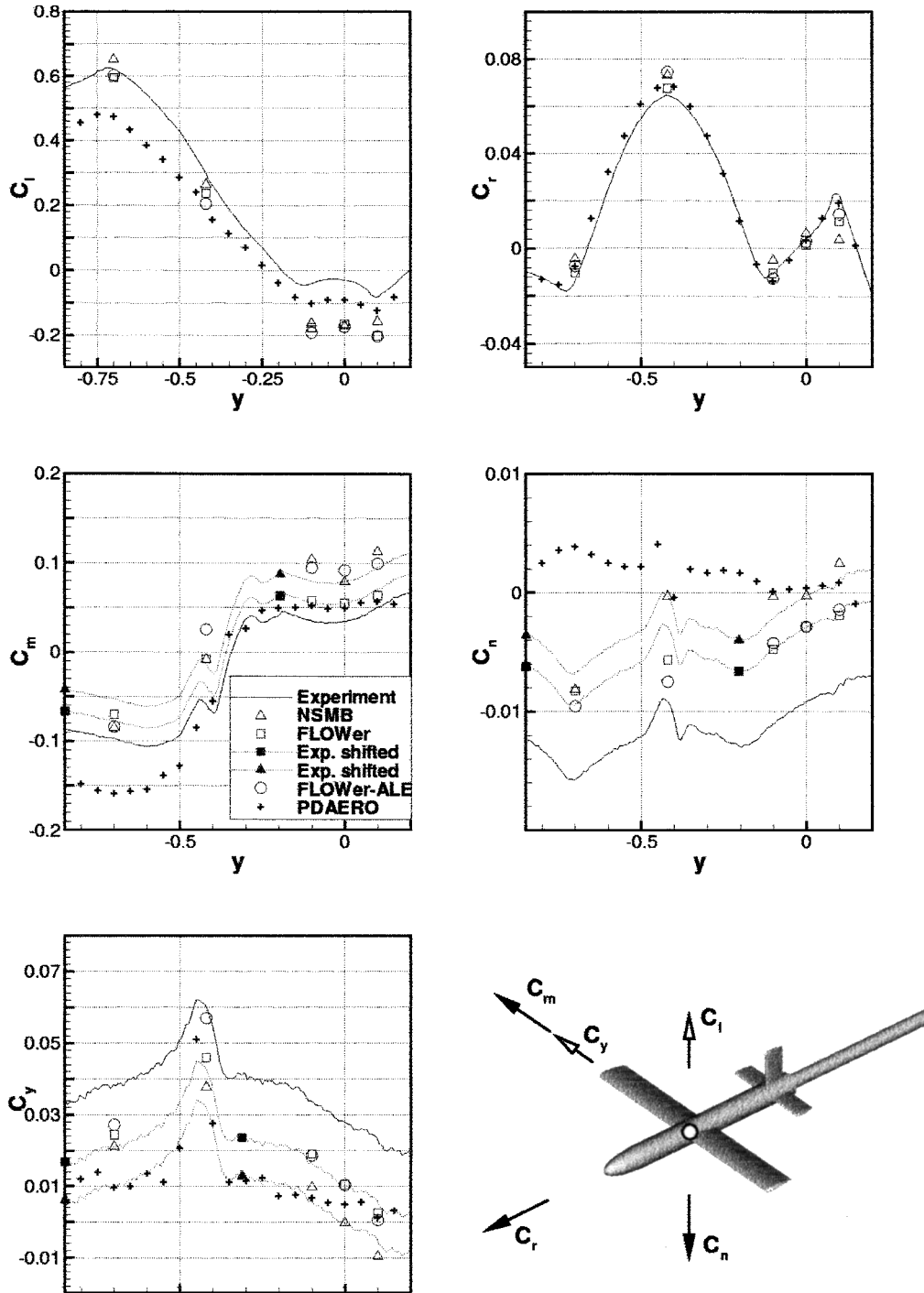
Fig. 14   Comparison of global force and moment coefficients; experimental results (DNW[2]), computational results with NSMB and FLOWer, and panel method results (PDAERO[17]). Dashed curves are experimental results, which are shifted.

allows the placement of so-called vortex transport meshes into the background mesh, which can be easily adapted to the vortices. Each of those additional meshes has 9.5×10^5 nodes. When started from a symmetric mesh of 3.4×10^6 nodes, the complete fine mesh has 5.3×10^6 nodes. For NSMB, a more time-consuming and costly process of remeshing is needed, leading to a grid with about 1.9×10^6 nodes.

A careful study shows that FLOWer needs eight cells in the core radius to be able to transport the vortex to the model. The fourth-order scheme coded in NSMB needs just two cells in the core. Figures 4 and 9 show that the change of the azimuthal velocities becomes small already at about $2r_c$, which means that from this point on a large stretching is permitted.

For the simplified methods, grid refinement is not necessary. With the transpiration method, the effect of the wake vortices on the airplane is introduced via the boundary conditions at the solid wall. The boundary condition changes from

$$v \cdot n = 0 \qquad \text{to} \qquad (v - v_i) \cdot n = 0 \qquad (12)$$

where v is the flow velocity, v_i the velocity induced by the vortex at the wall, and n the unit normal vector at the wall.

A generalization of the transpiration method is the ALE concept (see Ref. 18), where fluxes in the domain are modified. This method is normally used for moving grids, incorporating the grid velocity in the flux function at any place in the domain. In this case the inlet

vortex is imposed by modifying the fluxes from

$$
\begin{pmatrix} \rho \boldsymbol{v} \cdot \boldsymbol{n} \\ \rho \boldsymbol{v}(\boldsymbol{v} \cdot \boldsymbol{n}) + p\boldsymbol{n} \\ \rho E \boldsymbol{v} \cdot \boldsymbol{n} + p\boldsymbol{v} \cdot \boldsymbol{n} \end{pmatrix} \quad \text{to} \quad \begin{pmatrix} \rho (\boldsymbol{v} - \boldsymbol{v}_i) \cdot \boldsymbol{n} \\ \rho \boldsymbol{v}((\boldsymbol{v} - \boldsymbol{v}_i) \cdot \boldsymbol{n}) + p\boldsymbol{n} \\ \rho E (\boldsymbol{v} - \boldsymbol{v}_i) \cdot \boldsymbol{n} + p\boldsymbol{v} \cdot \boldsymbol{n} \end{pmatrix} \quad (13)
$$

where ρ is the density, p the static pressure, and E the total energy per unit mass.

Both methods have been implemented in the FLOWer code. Note that the simplified methods take the effect of vortices in the flowfield and on the model into account, but that feedback is missing. The vortex prescribed at the inlet is unchanged by interactions with the flow and on the model, contrary to real world events. This restricts its application to weak interactions. To verify the extent of applicability of this method, transonic two-dimensional flow around a NACA 0012 airfoil has been computed. The transpiration and ALE concepts have been compared to a reference solution. Instead of prescribing the angle of attack, corresponding induced velocities were prescribed. For small angles of attack, that is, a weak or absent shock, simplified results are good. For a higher angle of attack and a strong shock, $\alpha = 6$ deg and $M = 0.75$, the transpiration method fails completely, whereas the ALE solution is still very close to the reference solution.

The cases depicted in Fig. 11 were computed with an inlet Mach number of 0.171. Note that the computational inlet boundary is about 1 m from the model plane. Because the experimental field is given at the position of the model reference point, this means that the computation is more downstream than the position where the measurements of forces and moments on the trailing aircraft were taken. The NSMB solver uses the grid of Fig. 12 with refinements from the inlet plane to the model. Results were obtained after 1300 iterations. The FLOWer solver uses the grids of Fig. 13 for simplified ALE calculation and the enriched mesh for the full calculation. The results of the computations are summarized in Fig. 14. Included are results with the more economical panel method PDAERO.[17]

The discrepancy in the lift is not surprising after the the computation without vortices. The differences are largest when the nose of the model plane is between the vortices, which may indicate an incorrect modeling of the experimental flowfield. The panel method performs better in this region, but more strongly underestimates lift elsewhere. The coefficient C_R, which is related to the rolling moment, important from the pilot's point of view, is overestimated, but the general shape is well predicted. The coefficient C_D is computed without viscous drag and is, therefore, unreliable. For C_M, all methods are fairly far from the experimental data, and the computations just manage to capture the trend. The computation of C_Y and C_N, which are related to the horizontal force and the yawing moment, show a large shift with respect to experiment. The difference between computation and experiment is almost constant, which possibly indicates an offset problem. To check the sensitivity of the inlet conditions, computations were made with a change in the horizontal velocity of 2 m/s. This results in a rather small change of C_Y of about 0.005 and in C_N of about 0.003. This means that for the case $y = 0$, where the nose is between the vortices, the side force and moment should be roughly zero. Indeed, this is found in the computation, but not in experiment. The shift may be because the model sting support is asymmetrically mounted to the model support and too close to the aft part of the model. This induces sidewash velocities in the tail region area.[2] Apart from the shift, the inviscid computations give good results for C_N, whereas for C_Y the results are closer than with the panel methods. The discrepancy between the two Euler computations can be explained by the different treatment of the boundary conditions in the far field.

In general, the trends of the forces and moments are well captured. In spite of uncertainties in the modeling of the experimental flowfield, the inviscid computations manage to predict coefficients and moments of equal or better quality than the panel methods, albeit at a higher computational cost. An interesting result is that the simplified Euler method (FLOWer–ALE), which is not able to take the interaction between vortices and airplane into account, is in

fairly good agreement with the standard Euler methods. The influence of the airplane on the vortices seems to be negligible for most of the test cases considered, if global forces and moments are of main interest. An exception is the case shown in Fig. 11d, where the vortex is close to the thick fuselage instead of meeting a thin wing. Discrepancies are noticeable, for example, in the side force C_Y.

IV. Conclusions

The computation of a wake–vortex encounter with an inviscid solver raises the question of how accurate and how reliable the numerical results can be. We have tried to find an answer using a database from a well-controlled, accurate experiment in a wind tunnel. A very accurate representation of the experimental flowfield was needed to impose the upstream numerical boundary conditions for the solver. The decay of the tangential velocity of the main vortices with the distance was found to be proportional to $r^{-1/2}$. This excludes the use of a Lamb–Oseen vortex (see Ref. 3) and requires the more general analytical solution of Kirde.[5]

Two different Euler solvers were used to calculate the forces and moments that occur during a wake–vortex encounter. Both solutions are in fairly good agreement with each other and with results obtained by panel methods. Moreover, the discrepancies with experimental results are acceptable, given the inviscid assumption underlying the computations. Noticeable is overestimation of lift, which is common to inviscid computations. The roll is quite well predicted. In general, the trends of the forces and moments are well captured.

Better results may be expected by solving the Navier–Stokes equations, but it may not be easy to find an adequate turbulence model for this highly vortical flow where separation may occur at unforeseen places. Furthermore, the computational cost will be significantly higher.

References

[1]Ting, J. H., and Lan, C. E., "Navier–Stokes Calculation of Aerodynamic Characteristics of Wings in Vortex Wake Encounter," AIAA Paper 97-2267, June 1997.

[2]Hegen, G. H., "Wake Encounter Test in DNW Wind Tunnel—Test Number 98-1116," National Aerospace Lab., Rept. NLR-CR-98291, Amsterdam, June 1998.

[3]Lamb, H., *Hydrodynamics*, Cambridge Univ. Press, Cambridge, England, U.K., 1932.

[4]Saffman, P. G., *Vortex Dynamics*, Cambridge Monographs on Mechanics and Applied Mathematics, Cambridge Univ. Press, Cambridge, England, U.K., 1992.

[5]Kirde, K., "Untersuchungen über die zeitliche Weiterentwicklung eines Wirbels mit vorgegebener Anfangsverteilung," *Ingenieur Archiv*, Vol. 31, 1962, pp. 385–404.

[6]Boggs, P. T., Byrd, R. H., Rogers, J. E., and Schnabel, R. B., "User's Reference Guide for ODRPACK version 2.01," URL : http://www.netlib.org/odrpack/index.html.

[7]Moshier, S. L., "The CEPHES Library," URL: http://www.netlib.org/cephes/index.html.

[8]Lessen, M., and Paillet, F., "The Stability of a Trailing Line Vortex. Part 2: Viscous Theory," *Journal of Fluid Mechanics*, Vol. 7, No. 4, 1974, p. 769.

[9]Vos, J. B., Rizzi, A. W., Corjon, A., Chaput, A., and Soinne, E., "Recent Advances in Aerodynamics Inside the NSMB (Navier–Stokes Multiblock) Consortium," AIAA Paper 98-0225, 1998.

[10]Ducros, F., Laporte, F., Soulères, C., Guinot, V., Moinat, P., and Caruelle, B., "High-Order Fluxes for Conservative Skew-Symmetric-Like Schemes in Structured Meshes: Application to Compressible Flows," *Journal of Computational Physics*, Vol. 161, No. 1, 2000, pp. 114–139.

[11]Kroll, N., "National CFD-Project MEGAFLOW—Status-Report," *Notes on Numerical Fluid Mechanics*, Vol. 60, edited by H. Körner and R. Hilbig, Vieweg Verlag, Brunswick, Germany, 1997, pp. 15–23.

[12]Aumann, P., Barnewitz, H., Schwarten, H., Becker, K., Heinrich, R., Roll, B., Galle, M., Kroll, N., Gerhold, T., Schwamborn, D., and Franke, M., "MEGAFLOW: Parallel Complete Aircraft CFD," *Parallel Computing 27*, Elsevier, New York, 2001, pp. 415–440.

[13]Dougherty, F. C., "Development of a Chimera Grid Scheme with Application to Unsteady Problems," Ph.D. Dissertation, Stanford Univ., Stanford, California, June 1985.

[14]Benek, J. A., Buning, P. G., and Steger, J. L., "A 3-D Chimera Grid Embedding Technique," AIAA Paper 85-1523, 1985.

[15]Chessire, G., and Henshaw, W. D., "Composite Overlapping Meshes for the Solution of Partial Differential Equations," *Journal of Computational Physics*, Vol. 90, No. 1, 1990, pp. 1–64.

[16]Heinrich, R., and Kalitzin, N., "Numerical Simulation of Three-Dimensional Flows Using the Chimera-Technique," *Notes on Numerical Fluid Mechanics*, Vol. 72, edited by W. Nitsche, H.-J. Heinemann, and R. Hilbig, Vieweg Verlag, Brunswick, Germany, 1999, pp. 226–233.

[17]Brandsma, F. J., "Wake Encounter Computations for a Simple Configuration with the Panel Method PDAERO," National Aerospace Lab., Rept. NLR-TR-99441, Amsterdam, Oct. 1999.

[18]Donea, J., Giuliani, S., and Halleux, J.-P., "An Arbitrary Lagrangian–Eulerian Finite Element Method for Transient Dynamic Fluid–Structure Interaction," *Computer Methods in Applied Mechanics and Engineering*, Vol. 33, 1982, pp. 689–723.